# Synchrotrons as a Soft X-ray Source for Lithography

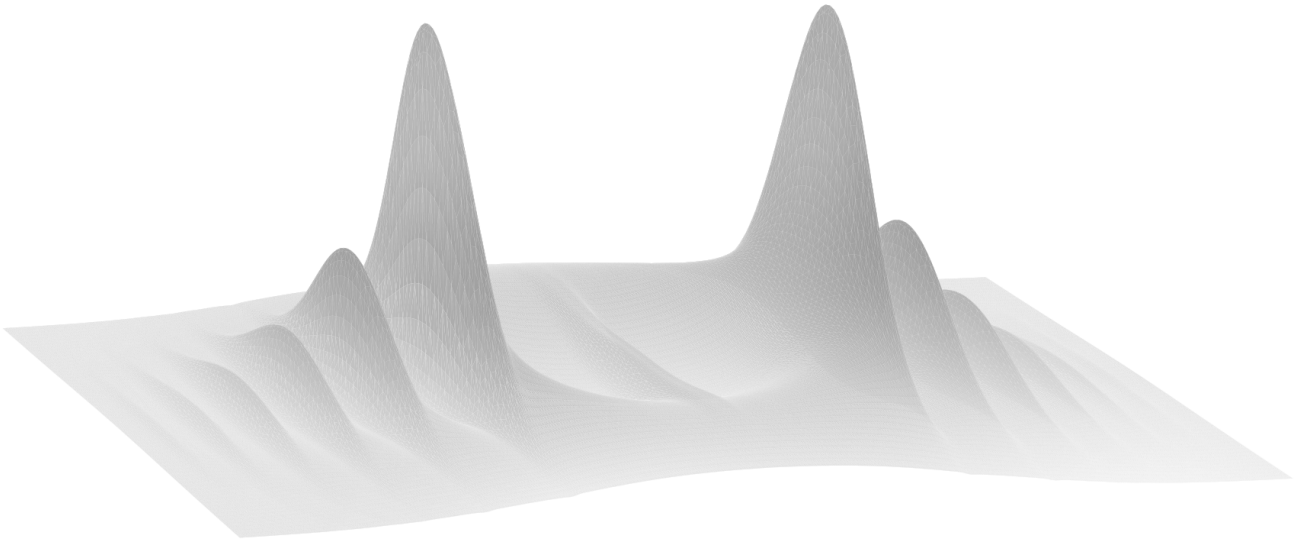

Author: Thomas Grandsaert
Supervisors: Andrey Shavorskiy, Hamed Tarawneh, Sverker Werin
Msc. - 4 months
Department of Physics
Division of Synchrotron Radiation
January 2021


LUND
UNIVERSITY

# Abstract

To move to lower modes in *extreme ultra-violet lithography* (EUVL) technology (and keep up with Moore's law), new sources of soft X-ray radiation must be developed. It is clear from previous studies that *Free Electron Lasers* (FELs) can easily meet the in-band power requirements at these lower wavelength modes, however detailed studies for insertion devices (undulators) as a *soft X-ray lithography* (SXL) source are due for a re-evaluation. Here we present the results of a systemic study to determine the undulator parameters to meet the required dosage, while meeting typical optical characteristics for wafer stages. To do this we resolved a large parameter set to find maximum in-band power at each wavelength mode. Using the resolved undulator parameters an accelerator lattice was developed to further realize the conceptual footprint of such a machine. Finally a cost-per-watt evaluation was made to estimate the total amount of power achievable per million euro. This showed that synchrotrons are an attractive and cost-effective source for SXL. However, a larger bandwidth and thus grazing incidence optics are required. Further developments of optical train feasibility will need to be performed.

# Acknowledgments

Thanks to Andrey Shavorskiy and Hamed Tarawneh for their guidance and support during this project. None of this would be possible of course without Sverker Werin and his efforts.

A special thanks goes out to the Swedish taxpayers, whose hard work enables dreams like mine becoming reality...

# Acronyms

| | |
|---|---|
| EUVL | Extreme Ultra-Violet Lithography |
| NA | Numerical Aperture |
| LINAC | Linear Accelerator |
| ML | Multi-Layer |
| KB | Kirkpatrick–Baez |
| SXL | Soft X-Ray Lithography |
| BW | Bandwidth |
| FEL | Free Electron Laser |
| LER | Line Edge Roughness |
| BAD | Basic Accelerator Design |
| ArF | Argon Fluoride |
| LPP | Laser Produced Plasma |
| SR | Synchrotron Radiation |
| ASML | Advanced Semiconductor Materials International |
| IMEC | Interuniversity Microelectronics Centre |

# Contents

# INTRODUCTION

Development of the semiconductor industry has been following *Moore's Law* for approximately 50 years, and the increase of transistor density is largely driven by significant advances in photolithography technology. In the late 1970's, the first lithographic system was developed for semiconductor wafers. This was done using the Mercury (Hg) "g-line" of 436 nm wavelength. This type of wafer stepper system was quickly popularized and promoted the efficiency of photolithography. Due to the Rayleigh criterion, a smaller wavelength of light must be used for the same optical system in order to achieve higher spatial resolutions. Higher spatial resolution means smaller feature sizes, and thus higher transistor density. Thus, the industry moved from 436 nm to an excimer laser for the Hg i-line (365 nm), then to krypton fluoride (248 nm), and then to argon fluoride (193 nm)[1].

At this point the industry was slated to move to even lower wavelengths, however the Rayleigh criterion states that higher spatial resolutions are also achievable with a larger *numerical aperture* (NA). Thus, instead of changing technologies again and moving to lower wavelengths, the industry began moving towards high-NA optical systems with argon fluoride scanners (ArF) and dramatically reducing feature sizes. The first commercial tool was developed and constructed in 2006 by ASML in the Netherlands[1].

The deployment of ArF scanners enabled the industry to reach 10nm and 7nm nodes. However, to move to nodes lower than 7nm, the industry has made the jump to laser-produced plasma sources (LPP). These sources work by exciting and relaxing inner electrons of highly ionized atoms such as tin (Sn). For tin sources the emission wavelength is *extreme ultra-violent* (EUV) light (13.5nm). At this wavelength, refractive lenses can no longer be used and reflective, *Bragg mirrors* must be used for the optical train. Thus, there was a small tradeoff for the NA, but a factor of $>10$ increase of spatial resolution due to decreased wavelength. Using this EUV technology, the semiconductor industry is hoping to push half-pitches using multi-patterning technology to below 3nm[1].

Despite the undeniable and resounding success of photolithography for semiconductor manufacturing, there remains much room for improvement. For example, the *line edge roughness* (LER) is much worse for EUV-based lithography (EUVL) due to the low resist dosages and secondary electron diffusion. Analogous to shot noise, one can improve the LER by increasing the resist dosage. However, the tradeoff is a reduction in wafer throughput, so to compensate one must increase the intensity (total flux) of the source.

Another significant issue is the cleanliness of the large collector mirror. Due to the fact that the light is being collected in a plasma environment, stray microparticles in the tin vapor contaminate the vacuum and accumulate on the collector mirror. This reduces the availability of the EUVL system due to the routine maintenance, and is a major challenge for the EUV industry[1].

Finally, a full wafer die is normally manufactured with a combination of multi-patterning and single-patterning for different layers. Multi-patterning is typically reserved for layers with half-pitches lower than 5nm. Lines at this size requires multiple exposure and etching steps for the same wafer layer. This is costly but increases overall performance. However, with a higher intensity source at a lower source wavelength, the multi-patterning layers at lower could be completed in a single step[1, 10].

It is clear that a light source which is cleaner and higher in intensity could potentially solve these problems. With this in mind, the EUVL community had previously explored the possibility of using other light sources. Of sources other than LPP considered, two which seemed promising included *free electron lasers* (FELs) and *synchrotrons*. Both of which are accelerators that use relativistic electrons

to produce light at the desired wavelengths of interest, called *synchrotron radiation* (SR). Even before EUVL was in production, almost 20 years ago, SR as photolithography source was studied by various experts in the field. The outcome of such studies is that SR which is *dipole* or *wiggler* based is not capable of producing the required intensity. However there was some promise of *undulator* sources meeting the intensity requirements and, demonstrably, FEL sources as well[13].

Since these initial considerations however, much has changed in accelerator and EUVL technology. In February 2020, IMEC and ASML have announced the single-exposure printing of 24 nm (12 nm half-pitch) lines using an ultra-high NA of 0.55. This was completed with a resist dosage of 34 $mJ/cm^2$, and is expected to be available for a production machine in 2022. It is likely this the source for such a machine will be ~250-500W @ 13.5nm[14]. At this point it seems clear that the increased numerical aperture approach has been successful, but is reaching its' technical limits. In addition, since the minimum feature size for any NA is $\lambda/2$, in order to get smaller pitches than 6.7 nm in single-exposures, it is inevitable that one must eventually decrease the source wavelength. It is the need for high intensity at wavelengths lower than EUV (soft X-rays), that makes SR sources begin to seem attractive again. Knowing this and the fact that accelerator technology has made broad leaps in the past 20 years, there is an increased likelihood that SR could fill the growing need for an intense soft X-ray lithography source. This would simultaneously decrease the minimum single-exposure line-width, while solving the aforementioned issues of cleanliness. Thus, the purpose of this thesis is to re-examine the feasibility of SR sources for lithography at soft X-ray wavelengths, from a practical viewpoint.

### Thesis work

The final deliverable of the thesis work was a cost-per-watt evaluation, as well as the conceptual footprint for a storage ring which could meet the requirements for *soft X-Ray lithography* (SXL). After reviewing relevant literature and recent publications on the state of EUVL, the thesis work could begin. The first step was a careful selection of wavelengths, based on various factors such as wavelength-dependent optical efficiencies or resonance lines of chemical resists. These are very important because it will define the beam energy for the succeeding steps. Following this selection, a large undulator parameter space was created in Python in order to find parameters which deliver the maximum flux at a particular wavelength of interest. Once the undulator parameters were evaluated, the study could continue by using the selected beam energy to create a lattice and finally a full conceptual footprint for the storage ring. The lattice was then used to find the natural emittance of the ring as well as the beta and dispersion functions. Using these and the aforementioned undulator parameters, the study moved on to the numerical simulations in SPECTRA[12], which were used to evaluate the total flux output for the wavelengths of interest, as well as flux densities. At this point it was clear that the study results varied greatly based on the selected bandwidth around the wavelength of interest. Therefore various bandwidths were also considered. Following these simulations, the final cost-per-watt evaluation could be created, again for various bandwidths.

## 1.1 Synchrotrons

*Synchrotrons* are particle accelerators which are typically designed to meet demanding brightness requirements for various diffractive, spectroscopic and imaging experiments. Also known as storage rings, they can vary greatly in size and energy. The phenomenon at the core of synchrotron storage rings is synchrotron radiation. This effect occurs when charged particles traveling velocities comparable to the speed of light are forced to change direction under the action of a magnetic field (Lorentz force). The particles in their new trajectory emit a cone of synchrotron radiation (or light). A diagram is shown in figure 1. Only electrically charged particles emit synchrotron radiation.

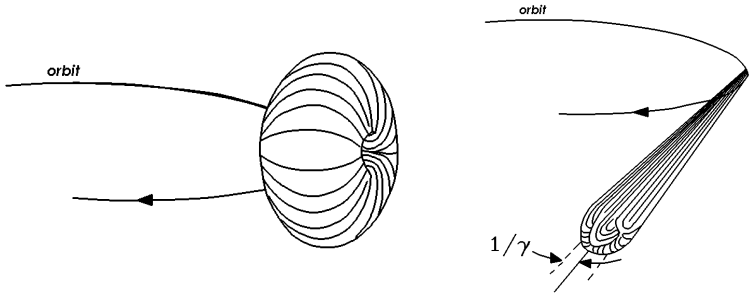


Figure 1: Synchrotron light emission for the (a) electron reference frame and the (b) laboratory frame

A synchrotron typically begins with a "gun" where the electrons are generated, followed immediately by a long series of RF-powered accelerating structures, which increase the velocity and energy of the electrons. The energized electrons are then transferred to the actual storage ring and subsequently oscillated back and forth by *insertion devices* to create light with the desired properties of the experiment.

**Hill's Equation**

Circular beam transport systems (ie: storage rings) are modeled by *Hill's differential equation,* which is a way to model movement of particles through periodic focusing elements, and is not dissimilar from a harmonic oscillator with a variable spring constant[3]:

$$x''(s) + K(s)x(s) = 0 \tag{1}$$

where $K(s)$ is the focusing function. This nominal particle model assumes the particle has no momentum deviation (ie: $\frac{\Delta p}{p_0} = 0$). Using *Floquet's theorem,* one can find the solution for equation eq 1 as[3]:

$$x(s) = \sqrt{\epsilon}\sqrt{\beta(s)}cos\left[\Psi(s) + \phi\right] \tag{2}$$

where $\epsilon$ is the *emittance,* $\beta$ is the *beta function,* $\Psi$ is the *betatron phase advance* and $\phi$ is the initial phase. This is a powerful result which yields matrices and linear coefficients as the model for tracking particles through a periodic focusing optical lattice[3].

### Beta Functions

The *beta function* is a function used to compute the transverse root mean square size of the particle distribution in phase space at the location $s$ along the nominal beam trajectory. Because particle beams are populations of particles, it is practically defined in statistical terms where a Gaussian distribution is assumed. Assuming a standard deviation of $\sigma$, the Beta function is related to the transverse emittance and particle positions via[3]:

$$\sigma_x(s) = \sqrt{\epsilon \cdot \beta_x(s)} \qquad \sigma_y(s) = \sqrt{\epsilon \cdot \beta_y(s)}$$

where $s$ is the longitudinal location, $\beta_x(s)$, $\beta_y(s)$ are the beta functions in $x$, $y$ transverse directions, and $\sigma_x$, $\sigma_y$ are the standard deviations in particle position projected along the selected transverse direction. Similarly, $\gamma_x$(s), $\gamma_y$(s) are related to the transverse emittance and particle angles via[3]:

$$\sigma_{x'}(s) = \sqrt{\epsilon \cdot \gamma_x(s)} \qquad \sigma_{y'}(s) = \sqrt{\epsilon \cdot \gamma_y(s)}$$

where $\sigma_{x'}$, $\sigma_{y'}$ are the standard deviations in particle angle, again for the projected particle directions $x$ and $y$.

### Dispersion Function

We must account for our particles being distributed with random deviations in momentum, for which Hill's equation becomes inhomogeneous[3]:

$$x''(s) + K(s)x(s) = \frac{1}{\rho}\frac{\delta p}{p} \tag{3}$$

If we define a special case where $\frac{\Delta p}{p_0} = 1$, we arrive at a solution for eq 3: [3]

$$\eta''(s) + \frac{1}{\rho^2}\eta(s) = \frac{1}{\rho} \tag{4}$$

where $\rho$ is the *dipole* bending radius, and $\eta(s)$ is the *dispersion* function, which takes the value of a scaler constant at every location along the lattice. This function, as well as the particles' individual momentums, must be included in the transfer matrices in order to fully define the movement within the optical lattice.

### Beam Emittance

Beam emittance is a useful property of particle beams inside accelerator systems, and can be measured longitudinally and transversely. It can be characterized as the collective positions and directions of a selection of particles, and is used to qualify many aspects of the machine including the performance of the optical system and the lattice model. It is also used to calculate the output cone of the synchrotron light exiting undulator systems. Transverse emittance is usually calculated as the spread of particle position and angle in transverse *phase space* (figure 2)[3]. In this figure $\beta$ is the beta function, $\alpha = \frac{\beta'}{2}$ and $\gamma = \frac{1+\alpha^2}{\beta}$.

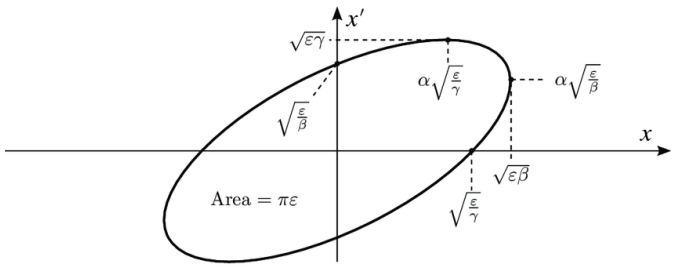


Figure 2: Phase space diagram. Here $x$ and $x'$ represent the position and angle, respectively, in one transverse direction [4]

**Dipoles**

Normally in beam optics simulations the focusing strength is normalized for the particle energy. However for the purposes of this study the beam energy is important to determine the overall footprint of the machine. Specifically, the 'magnetic rigidity' equation is useful for finding the bending radius of the dipoles[3]:

$$B\rho[T \cdot m] = \frac{10}{2.998}\beta E[GeV] \tag{5}$$

where $\rho$ is the bending radius, $B$ is the magnetic field, $\beta$ is relativistic beta and $E$ is the electron energy.

## 1.2 Undulators

While there are various types of insertion devices, this discussion will focus on *undulators*. Undulators are periodic magnets which are inserted into the path of the electron beam and, (via the Lorentz force) cause many transverse deflections in the path of the electrons. This deflection is normally manifested through permanent magnets, but electromagnets can also be used. Typically the length of each magnet is 2-5 cm, and the total length of the undulator device is approximately 2-5 meters. This means that the electron will interact with ~50-200 periods before exiting the undulator, depending on period length. In the process of each interaction, the electrons emits synchrotron light in the (mostly) forward direction.

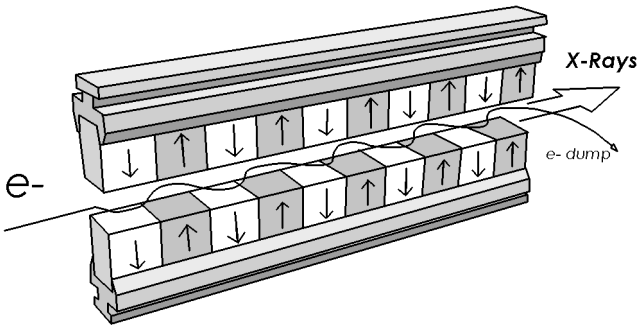


Figure 3: An undulator is essentially an array of periodic magnets

### Deflection Parameter

One of the most important parameters for any undulator is the *deflection parameter, K,* which categorically represents the amount of transverse displacement that a passing electron will exhibit. $K$ affects multiple characteristics of the output radiation from any undulator device. These include power distribution in different harmonics, total power, output radiation angle, and the fundamental harmonic wavelength[2].

$$K = \frac{B_0 e}{m_0 c} \frac{\lambda_u}{2\pi} = 93.36 B_0 \lambda_u \tag{6}$$

$B_0$ is the field strength inside the undulator and is represented in units of T. $\lambda_u$ is the undulator period and is in units of m. The constants represented are $c$, the speed of light, $e$, the electron charge and $m_0$, the electron rest mass. The parameter $K$ itself is dimensionless. At this point it is important to note that the alignment of the two periodic magnetic "jaws" can change the polarization and spectral output of the undulator radiation. If the fields are not vertically aligned like in figure 3, a nonzero deflection parameter in the $y$ plane is introduced, which leads to the necessary distinction between $K_y$ and $K_x$. This also changes the polarization of the output radiation from linear to elliptical. Eventually as $K_x \approx K_y$, the polarization becomes circular, and thus the phase between $x$ and $y$ planes is $\phi = \frac{\pi}{2}$.

### Undulator equation

The electrons being deflected in their path are emitting radiation like a magnetic dipole. However, because they travel very close to the speed of light there must be a Lorentz transformation to accurately calculate the cone of light emitted in the laboratory frame of reference. Also, because the electrons are emitting uniformly throughout their deflected path, the wavefronts will interfere constructively for different wavelengths at different angles. This is captured elegantly in the undulator equation[2]:

$$\lambda = \frac{\lambda_u}{2n\gamma^2} \left(1 + \frac{K^2}{2} + \gamma^2 \theta^2\right) \tag{7}$$

where $\gamma$ is the relativistic gamma, $n$ is the harmonic of interest, and $\theta$ is the viewing angle with respect to the beam, axis. For a helical undulator the equation is slightly different:

$$\lambda = \frac{\lambda_u}{2n\gamma^2} \left(1 + \frac{K_x^2}{2} + \frac{K_y^2}{2} + \gamma^2 \theta^2\right) \tag{8}$$

where $K_x$ and $K_y$ are the deflection in $x$ and $y$ planes. For our case we are also interested in on-axis circularly polarized radiation ($K_x = K_y$), so the last term is omitted and the undulator equation 8 becomes[2]:

$$\lambda = \frac{\lambda_u}{2n\gamma^2} \left(1 + K^2\right) \tag{9}$$

### Harmonics

Undulators emit radiation at a fundamental wavelength as well as its' harmonics. Normally when viewing on-axis in planar undulators, even harmonics are well suppressed and only odd harmonics are transmitted. However the energy distribution across the harmonics changes with respect to the undulator parameter $K$. This is known as the energy distribution function[2]:

$$F_n(K) = \frac{n^2K^2}{(1+K^2/2)^2}\left(J_{(n+1)/2}(Y) - J_{(n-1)/2}(Y)\right)^2 \tag{10}$$

where $n$ is the harmonic, $J$ is the Bessel function and $Y = \frac{nK^2}{4(1+K^2/2)}$. $F_n$ is plotted for different planar undulator harmonics in figure 4[2]. For a helical undulator, we again split the deflection parameter, thus the energy distribution function, into its' respective transverse $x$ and $y$ planes, and $F_n$ becomes:

$$F_n(K_x, K_y) = \frac{n^2}{(1+K_x^2/2+K_y^2/2)^2}\Big(K_x^2\left(J_{(n+1)/2}(Y) - J_{(n-1)/2}(Y)\right)^2 + K_y^2\left(J_{(n+1)/2}(Y) - J_{(n-1)/2}(Y)\right)^2\Big) \tag{11}$$

where $Y = \frac{n\left(K_x^2-K_y^2\right)}{4(1+K_x^2/2+K_y^2/2)^2}$.

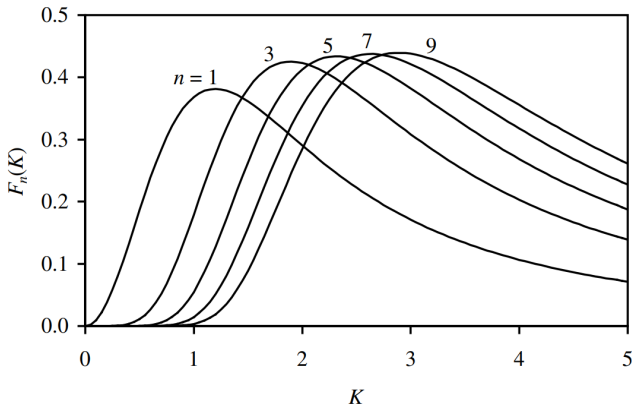


Figure 4: $F_n(K)$ for different on-axis undulator harmonics [2]

### Flux in the Central Cone

Normally the vertical opening angle of synchrotron radiation emitted by an electron in a single turn is approximated as $\sigma_{r'} \approx \pm\frac{1}{\gamma}$ However this becomes more complicated when considering many electrons and many periodic turns. To simplify, flux calculations are confined to an on-axis *central cone* of $\sigma_{r'} = \sqrt{\lambda/L}$. Using this, one can integrate flux for all electrons over all solid angles within the central cone and arrive at the equation for total flux per 0.1% bandwidth for a planar undulator [2]:

$$\dot{N} = 1.43{\times}10^{14} NIQ_n(K) \tag{12}$$

where $N$ is the number of undulator periods, $I$ is the beam current. The $Q_n$ term captures the quadratic dependence of flux output on the $K$ parameter, as well as then $K$ dependent energy distribution in the specified harmonic[2]:

$$Q_n(K) = \frac{1 + K^2/2}{n} F_n(K) \tag{13}$$

where $F_n$ is the energy distribution function as specified in eq 10. For a helical undulator, $Q_n$ becomes [2]:

$$Q_n(K_x, K_y) = \frac{1 + K_x^2/2 + K_y^2/2}{n} F_n(K_x, K_y) \tag{14}$$

Again, for a circularly polarized configuration, $K_x = K_y$. In this case $Y = 0$ and the only non-zero Bessel term in eq 11 occurs at $J_0$ or when $n = 1$. This means that only the fundamental harmonic is present on-axis and the integrated flux becomes[2]:

$$\dot{N} = 2.86{\times}10^{14} NI \frac{K^2}{1 + K^2} \tag{15}$$

**Total Power**

The power emitted from undulators can be quite considerable. It can even be enough to damage components and equipment. Therefore from a practical point of view it is important to consider the total integrated power across the wavelength spectrum when estimating undulator flux. By starting with the power emitted by a single bending relativistic electron, and integrating over the assumed sinusoidal dipole field of an undulator we can find estimated the total power for a planar undulator[2]:

$$P_{planar} = \frac{e^2 \gamma^4}{6\pi\epsilon_0} \int_0^L \frac{1}{\rho(s)^2} ds = 632.8 E^2 B_0^2 LI \tag{16}$$

where $e$ is the electron charge, $\gamma$ is the relativistic gamma, $\epsilon_0$ is the permittivity of free space, $\rho$ is the bending radius along the path $s$. Following the same logic for the case of a helical undulator, we find that the total power is exactly double that of a planar undulator.

$$P_{helical} = 1265.5 E^2 B_0^2 LI \tag{17}$$

**Field Strength v. Period**

For any given undulator, there is physical limit to the amount of field that can be achieved, given the gap between the magnets. This is one of the biggest limiting factors in undulator simulations, as it is this relationship which defines the maximum amount $K$ value for various beam energies. The maximum achievable field in a 2D projection for pure permenant magnets is estimated as[5]:

$$B_0 = a\, exp\left(-b\frac{g}{\lambda_u} + c\left(\frac{g}{\lambda_u}\right)^2\right) \tag{18}$$

where $g$ is the undulator gap, and $\lambda_u$ is the undulator period. $a$,$b$,$c$ are coefficients based on different permenant magnet materials. For different permanent magnet materials, typical values are tabulated in table 1.

| | $a$ | $b$ | $c$ |
|---|---|---|---|
| $SmCo_5$ | 3.33 | 5.47 | 1.8 |
| $NdFeB$ | 3.44 | 5.08 | 1.54 |

Table 1: Field v. period coefficients for typical permenant magnet materials [5]

This relationship is empirical in nature and based on a series of 2D field calculations[5]. The curve for maximum B-field of a NdFeB-based undulator is shown in figure 5.

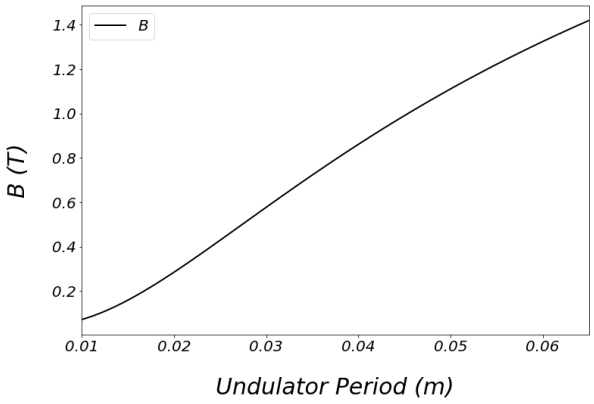


Figure 5: B-field max for a NdFeB-based undulator with a 12mm gap

## 1.3 Extreme Ultra Violet Lithography

*Extreme Ultra Violet Lithography* (EUVL) is a manufacturing process for chipmakers in the semiconductor industry. It begins with a silicon wafer which has a *chemical resist* deposited on the surface. Simply stated, the resist layer is irradiated with EUV light (typically $\lambda = 13.5nm$) in a particular pattern of interest. The damaged resist can then be chemically etched away to reveal the irradiated pattern. Typically to achieve smaller feature sizes, the process must be repeated multiple times with different mask patterns. The basic function behind the photolithography etching process is shown in figure 6.

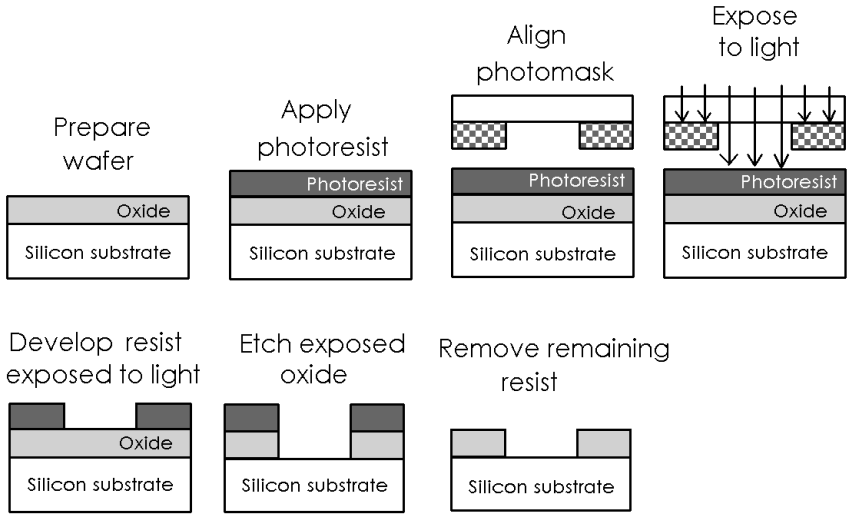


Figure 6: Basic photoresist function

**Light source**

Tin(Sn)-based laser produced plasma (LPP) is the source of EUV light in most modern lithography machines. This starts with a liquid spherical droplet around 100-200 $\mu m$, which is reshaped into an extended disk shape with a laser pre-pulse (figure 7). The droplet is then irradiated with a main laser pulse, which then creates the highly ionized, EUV emitting tin plasma. The process is dependent on an extremely intense, multi kilowatt $CO_2$ laser[8].

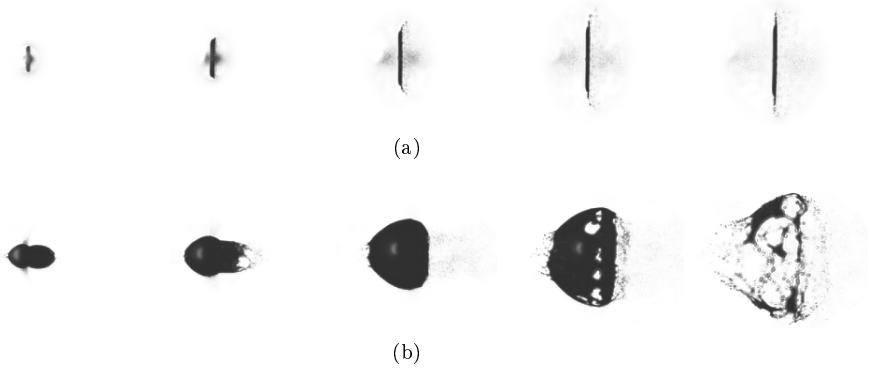

(a)

(b)

Figure 7: Shadowgraphs of tin droplets at 0.5 $\mu s$, 1 $\mu s$, 2 $\mu s$, 3$\mu s$, 4 $\mu s$ for (a) 15mJ and (b) 4 mJ laser pre-pulses. With a sufficient irradiation dose (~15 mJ), the tin droplets extend into a disc shape which is ideal for the second main laser pulse, generating intense EUV emission. [8]

**Optical train**

The optics of a LPP source begin with a large a collector mirror very close to the light-emitting plasma. This is due to the fact that the plasma-produced light has a wide angular spread. Following the collector mirror, the light enters a vacuum window where it is then collimated and guided through the *illumination optics*. It is after the illumination optics that the light is reflected off the *reticle mask,* which contains the patterns to be etched. The light is guided through the *projection optics* and finally on to the wafer.

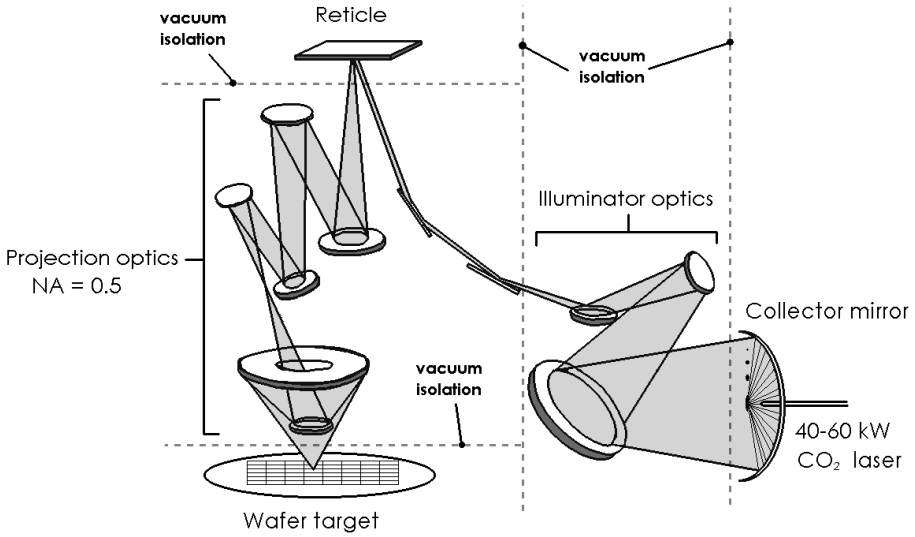


Figure 8: EUVL optical train

One of the most important characteristics of any lithographic optical system is the *numerical aperture* NA. This can be simply described as the range of exit angles coming off of the final lens in the *projection optics*. For lithography, a higher NA means a more intense flux density on the wafer surface with a larger solid angle, meaning the required exposure dose can be reached in a shorter time. A shorter dosage time means higher wafer throughput, and less cost-per-watt. Higher NA also enables higher *resolution*, even if it is done in multiple exposures. The optical tradeoff for a higher NA is lower depth of focus.

#### Pitch

The *pitch* or *half-pitch* of features in a chemically etched silicon wafer are the smallest resolvable feature size in a lithography process. This can be the result of multiple exposure/etching cycles, but in general the lowest possible pitch is dependent on wavelength $\lambda$ of exposure light and the numerical aperture NA:

$$Pitch \propto \frac{\lambda}{NA}$$

This means that in order to decrease pitch (or increase resolution), one can either lower the exposure wavelength or increase the NA. In conventional EUVL, moving to lower wavelengths of light has presented significant technical challenges. Thus the strategy for moving to smaller pitches (and thus more transistors) in recent years is primarily focused on increasing the numerical aperture. The goal of this study is to focus on providing a solution which decreases the wavelength as well as preserving a high NA.

## 1.4 Optics

#### Spatial coherence

Spatial coherence describes the capacity for two points in space to interfere over time. In technical terms it is described as the *cross-correlation* between two points in a wave for an extended time period. Where cross correlation is the sliding dot product of two signals[6].

#### Multi-layer mirrors

Multi-layer (ML) mirrors (also known as *Bragg* mirrors) are mirrors which function using a series of thin dielectric materials in order to create constructive interference. This is achieved by making sure the path-length difference for reflecting layers is one integer value of the desired wavelength at a particular angle. By selecting the thickness and material carefully, relatively high reflectivities can be achieved[6]. A diagram is shown in figure 9b.

In typical EUVL optical trains, almost every mirror used is a ML mirror. In the working wavelength (13.5nm), the reflected bandwidth is relatively small at around 2%, and the reflectivity is typically around 70%. At the end of the optical train, the resultant power on the wafer is 4% or lower. The advantages of using such mirrors is that they can have almost normal incidence to each other in the optical train, leading to a smaller total size. They also can easily create higher numerical apertures, which is critical for smaller pitches. As wavelengths decrease, the reflectivity of ML mirrors is diminished[6].

### Grazing-incidence mirrors

Another method for X-Ray optical propagation is grazing incidence (or reflection optics). X-Rays can be reflected off smoother surfaces with a metallic coating at very shallow angles. These shallow angles are known as *grazing incidence*. The reflections are very efficient for high-density metal elements like Au, Pt, and Ir. Similarly to optical reflections, this effect is non-dispersive. This means that a wider bandwidth can be focused via grazing incidence, as long as the angle remains below the so called *critical angle*. The critical angle is the angle where total external reflection occurs. Above this angle exhibits diminishing reflectivity for a given wavelength. Usually grazing incidence mirrors are utilized in pairs called *Kirkpatrick-Baez* (KB) mirrors. A diagram of KB mirrors is shown in figure 9a.

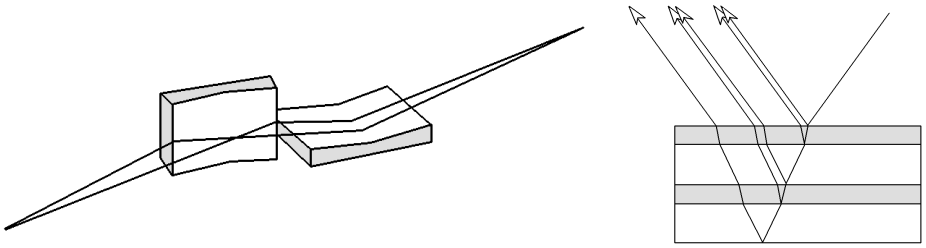

(a) (b)

Figure 9: (a) KB mirror and (b) ML mirror functionality

# SOFTWARE AND METHODS

## 2.1 Parameter optimization

It was determined that the parameter optimization should begin under various assumptions. The first, most obvious, being that user will want the maximum amount of flux at a certain wavelength of interest, in the central cone, in the first harmonic. Another assumption is that, contrary to typical synchrotron requirements, peak brightness is not critical. Also, due to the relatively small size of the machines, the beam emittance will not be small enough to accommodate in-vacuum undulators. Therefore all undulator calculations should assume out-of-vacuum gaps ($\geq 12mm$).

To begin the first step of maximizing the in-band flux for all possible wavelengths, the following parameter space was created in Python:

| **Parameter** | **Start** | **Stop** | **Pts** | **Unit** |
|---|---|---|---|---|
| *gap* | 12 | 12 | (1) | mm |
| *Energy* | 1 | 2 | (81) | GeV |
| *current* | .5 | .5 | (1) | A |
| $\lambda_u$ | 3 | 5 | (61) | cm |
| $L$ | 20 | 20 | (1) | m |
| $B$ | 0.1 | 1 | (61) | T |

where the *Pts* column refers to the number of steps between the start and the stop points. It was quickly apparent that the maximum in-band flux occurs at the minimum gap, thus it was chosen to remain fixed at 12mm to reduce further computational times. The energy of 1-2 GeV was chosen because it is possible to maximize flux for all wavelengths of interest (defined below) in this range, assuming a certain minimum undulator period. A lower limit of 3 cm for the undulator period was selected for practical manufacturing purposes. The beam current was selected based on what is normally achievable in modern storage rings. The magnetic field range was chosen based on normal undulator field limitations. Finally, the length was chosen to be 20 m, knowing that any resolved flux can be scaled linearly by the length of the undulator.

Each permutation of this parameter space was run through a set of Python functions which calculate the undulator characteristics of interest. These include the output radiation wavelength $\lambda_\gamma$ (eq. 9), deflection parameter $K$ (eq. 6), maximum possible field $B$ (eq. 18), approximate energy distribution $F_n$ (eq. 10), total power (eq. 16, 17), and the flux in the central cone in the first harmonic (eq. 12, 15). The evaluated parameters were cross-checked in SPECTRA in section 2.3.

The evaluated parameter sets were then stored in a pandas (a Python-based data science package) data-frame which could be easily organized based on the parameters of interest. In this case we were mostly interested in the fundamental wavelength $\lambda_\gamma$ and the central cone flux. It would become apparent later in the study that it is necessary to push the fundamental to a higher energy (lower wavelength) in order to get more flux under a given bandwidth. Various parameter sets for different bandwidths are given in tables 4, 12, 13 of the result sections.

Due to the fact that polarization of the output undulator radiation is not a critical for photolithography, circular undulators were selected as the primary focus of the rest of the study. This is because of two main advantages. The first is that a circular undulator would produce higher output radiation for a lower K value, and the second being the suppression of higher harmonics on-axis. Harmonic suppression means less "contamination" of the output radiation of interest.

**Wavelength selection**

The desirable wavelength for the undulator output radiation is a critical step. With the knowledge that atomic cross-section generally decreases with photon energy, it was decided that prospective lithographic processes should work around resonance wavelengths for organic photoresists. Thus, various common photoresist elements were selected including sulfur, nitrogen, carbon and oxygen. The attenuation curves for these elements are shown in figure 10.

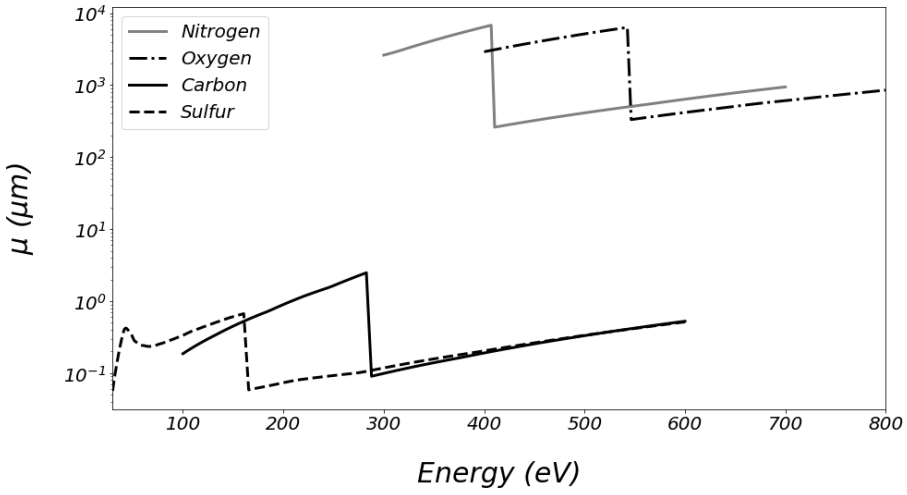


Figure 10: Absorption length v. energy for sulfur, carbon, nitrogen, oxygen [11]

## 2.2 Lattice design

After a set of desireable undulator parameters were found, the beam energies could be used to develop an accommodating *accelerator lattice* concept. This would provide a two-fold input for the study. First, it gives an idea of the relative size of the machine, which would be useful for the cost study. The second is that it helps to estimate the storage rings' natural emittance, as well as the beta and dispersion functions, which are useful input for the SPECTRA simulations in section 2.3. It was also intended from the start of the project that the first, most basic machine design should be a racetrack shape. This was intended to minimize the footprint at the same time maximizing output flux.

A parametric lattice design software called Basic Accelerator Design (BAD)[19] was used to develop 1/2 of the intended racetrack shape. This included three dipole magnets as well as periodically focusing and defocusing magnets. The undulators were represented as four meter long drifts, with focusing magnets in between. It was assumed that the dispersion function should be zero at the undulator entrance. This is because the undulators are essentially periodic dipoles, which with high dispersion would cause undesirable destructive interference at the undulator output. The beta functions as well as the dispersion function in the $x$ transverse plane are shown in figure **??**. The specific optical focusing parameters are tabulated in table 2, and the storage ring parameters which are important for the SPECTRA numerical simulations are tabulated in table 3. These represent the beta and dispersion functions at the undulator entrance as well as the emittance in the $x$ transverse plane, also known as the natural emittance. For the figures and table in this lattice concept, the beam energy was 1.2 GeV. It is important to note that optical focusing parameters are normalized for the beam energy, however the length of the dipoles needs to be adjusted according to the beam energy. Using the magnetic

rigidity equation 5 along with the resolved beam energies in table 4, the bending radius can be found and thus the total required dipole length determined.

| | | $Q_{f_1}$ | $Q_{d_1}$ | $Q_{f_2}$ | $Dip_a$ | $Q_{d_2}$ | $Dip_b$ |
|---|---|---|---|---|---|---|---|
| $k_{dip}$ | [1/m] | 0 | 0 | 0 | 0 | 0 | 0.33 |
| $k_{qua}$ | [1/m] | 0.101 | -3.36 | 3.85 | 0 | -2.71 | 0 |
| $L$ | [m] | 0.2 | 0.2 | 0.2 | 3 | 0.2 | 3 |

Table 2: Lattice element focusing parameters rounded to the second decimal

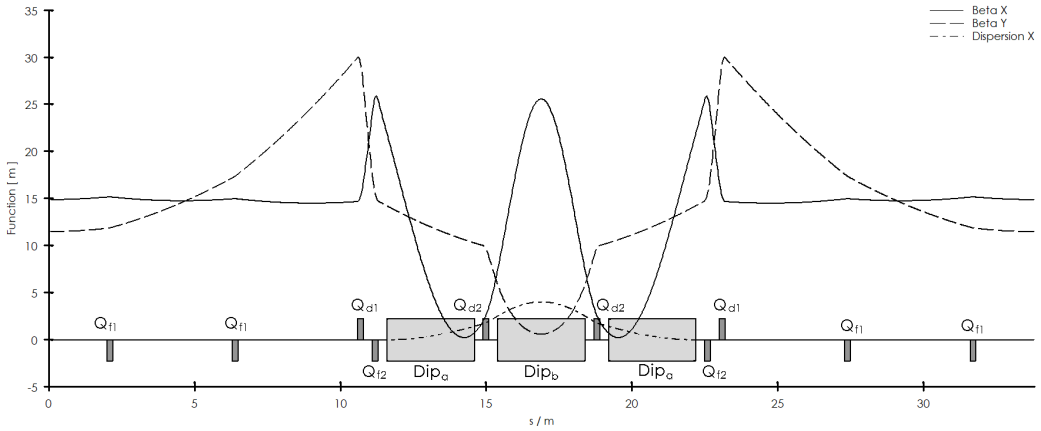


Figure 11: Lattice design for a 20 m undulator system. Here $Q_{d1,2}$ : quadrupoles [defocusing], $Q_{f1,2}$ : quadrupoles [focusing], $Dip_{a,b}$ : dipoles. The undulators are located in the long drifts in between the quadrupoles at 0-10 m, and 23-35m.

## 2.3 SPECTRA

### Setup

With a conceptual lattice developed one can move forward to simulate the total flux numerically. The software chosen for this calculation was SPECTRA, which is a trusted code within the field of synchrotron science. The evaluated undulator parameters as well as electron energy, dispersion and beta functions from the lattice were used as input parameters for the SPECTRA code. The storage ring parameters are shown in table 3. The parameters include the beam current $I_{avg}$, beta functions $\beta_x$ / $\beta_y$, dispersion function $\eta_y$, circumference $C$, number of bunches, natural emittance $\epsilon_{natural}$ (or $\epsilon_x$), longitudinal bunch length $\sigma_z$, and energy spread $\sigma_\delta$. It is important to note that the number of bunches assumes a RF frequency of 100 MHz and can be calculated via the harmonic number $h = \frac{f_{RF}}{f_{rev}}$, where $f_{rev}$ is the electron revolution frequency. A reasonable longitudinal bunch length and energy spread were assumed, based on the the MAX IV design report[7].

| $\beta_x$ | $\beta_y$ | $\eta_y$ | $\epsilon_{natural}$ | $I_{avg}$ | $C$ | *bunches* | $\sigma_z$ | $\sigma_\delta$ |
|---|---|---|---|---|---|---|---|---|
| [m] | [m] | [m] | [m.rad] | [mA] | [m] | | [mm] | [%] |
| 15 | 12 | 0 | 2.5e-07 | 500 | 58 | 20 | 35 | 0.08 |

Table 3: Evaluated storage ring parameters for SPECTRA

### Flux through an aperture

The first and most important simulation is the total flux through a circular slit aperture, as shown below in figure 12.

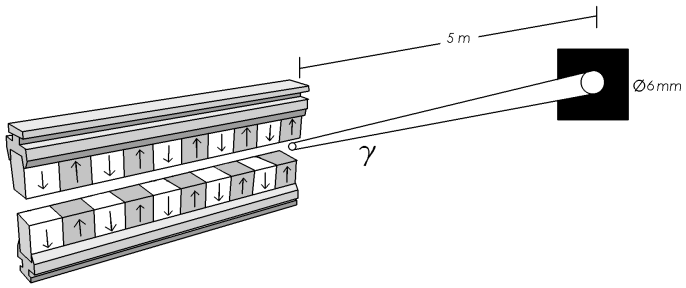


Figure 12: Setup for total flux simulation

The aperture effectively filters out the lower energy tail of each undulator harmonic. It is noted here that a larger aperture radius could be chosen to increase the overall in-band flux by as much as 50%, with the negative tradeoff of larger out-of-band radiation through the mirror system. Practically, any aperture size would require strong cooling, because of sizeable heat loads on the order of a several kW. Total flux through various aperture diameters is also show in figure 13. In our case the distance chosen for the slit was 5 meters from the end of the undulator and the diameter 6 mm based on a survey of various aperture sizes shown in figure **??**. With the aperture selected, it was important to push the undulator harmonic higher than the nominal energy by $\sim \frac{eV}{\frac{1}{2} \cdot BW}$, in order to maximize the total integrated flux. The simulation results were post-processed in Python in order to find the in-band power for various bandwidths.

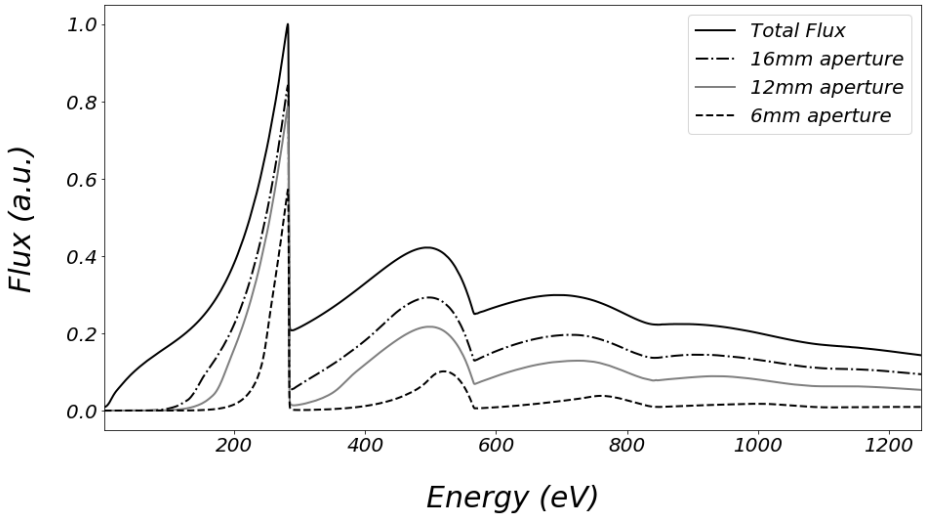


Figure 13: Normalized spectral output for various apertures at a distance of 5 meters, with the fundamental at 280 eV

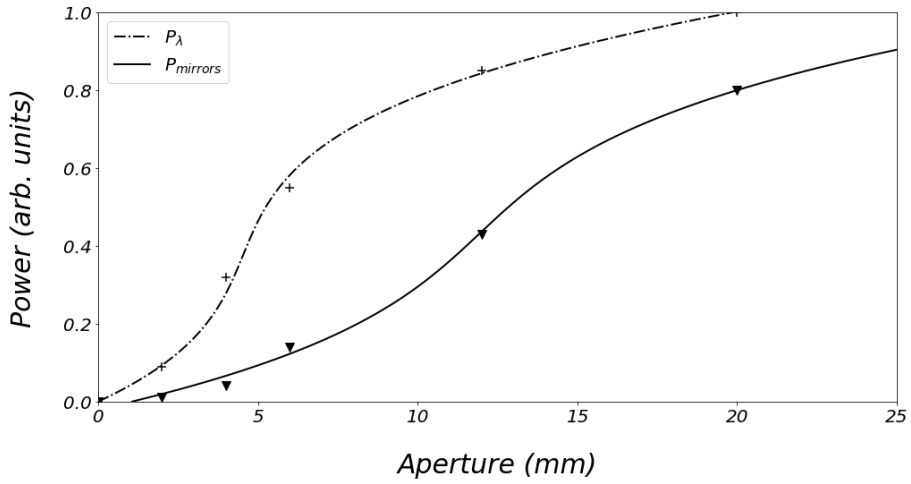


Figure 14: Normalized in-band output power $P_\lambda$ (10% BW) v. aperture size at 280 eV. It is also desirable to minimize unnecessary out-of-band power on the mirror system $P_{mirrors}$. Thus, normalized power onto the mirrors is also shown. Data for this figure is shown in Appendix C

**Flux Density**

It is also important to understand the flux density profile of the emitted undulator radiation. This could be important for determining the type of mirror shape which could accommodate the beam and the heat load at various points. A flux density calculation was therefore performed in SPECTRA for various bandwidths around the fundamental for the wavelengths of interest. This was performed by stepping through an energy range, evaluating the flux density at each step, and then summing the outputs for various bandwidths in $x$' and $y$' using Python.

## 2.4 Post-processing

It is important to note that most calculations in SPECTRA are integrated for a bandwidth of 0.1%. While making sure the granularity of SPECTRA output files is 0.1 eV, which is far below this bandwidth, it is important that all summation functions across the selected bandwidths are in 0.1% steps of the wavelength of interest. For the flux-through-aperture simulations the summation is performed across a 1D curve. For the flux density simulation the summation is performed across multiple 2D grids, with each grid again representing a step of 0.1% with respect to the wavelength of interest.

**Conceptual footprint**

Between the lattice design and the undulator parameters the conceptual footprint was developed for various beam energies. These were drawn visually with a 40 m undulator on a racetrack storage ring. The LINAC length was determined under the assumption that a typical accelerator has a field gradient of ~24-25 MeV/m. The size of the storage ring radius was determined using the magnetic rigidity equation 5.

**Power v. cost**

Using the outputs from the partial flux simulations as well as an internal MAX IV cost sheet, the cost-per-watt analysis could be performed. The cost sheet includes the material cost for the 1.5 GeV storage ring, including the following line items:

- System design
- Magnets incl. protection system
- Girders
- RF transmitters, cavities and low level
- Injection system
- Vacuum systems and pumps
- Diagnostics
- Cooling and cables

The total cost of the magnets, diagnostics and vacuum systems were scaled according to the ratio between the MAXIV storage ring circumference and the circumference of the conceptual footprints.

# RESULTS

## 3.1 Resolved undulator parameters

The resolved undulator parameters for 2% BW is shown in tables 4. Although the overall power is increasing with an increasing wavelength, the total flux remains fixed at around 3e+16 ph/s @ 0.1%BW. This is because in the case of a fixed beam current, the flux is limited by the number of undulator periods, and the undulator deflection parameter. The latter of which is defined by the field v. period curve shown in figure 1. It is important to note again this curve is heavily dependent on the gap, which remains fixed at 12mm. Thus, it seems natural that the maximum flux would be found close to the lowest possible undulator period, which maximizes the number of electron deflections along the undulator according to equation 15. As stated previously, in order to maximize the flux under a certain bandwidth, the fundamental must be pushed to a higher energy by $\sim \frac{eV}{\frac{1}{2}\cdot BW}$. Thus, the parameter sets for 2%, 4%, 10% BW are shown in appendix E.

| $E_{e-}$ | $\lambda_\gamma$ | $K$ | $B$ | $\lambda_u$ | $\Phi_{1st}$ | $\mathbf{P_{1st}}$ | $\mathbf{P_{total}}$ |
|---|---|---|---|---|---|---|---|
| [GeV] | [nm] | | [T] | [cm] | [ph/s @ 0.1%BW] | [W @ 0.1%BW] | [kW] |
| 1.14 | 7.75 | 1.183 | 0.4 | 3.17 | 2.89e+16 | 0.75 | 2.62 |
| 1.45 | 4.43 | 1.163 | 0.415 | 3.0 | 3.01e+16 | 1.37 | 4.58 |
| 1.76 | 3.1 | 1.182 | 0.415 | 3.05 | 3.01e+16 | 1.94 | 6.77 |
| 1.95 | 2.34 | 1.121 | 0.4 | 3.0 | 2.92e+16 | 2.50 | 7.70 |

Table 4: Resolved circular undulator parameters used for 2% BW simulations in SPECTRA ($I = 500$ mA, $L = 20$ m, gap = 12 mm)

## 3.2 SPECTRA outputs

The in-band power output for various bandwidths and output wavelengths are tabulated in table 5. Again here we see the same trend that the power is increasing for lower wavelengths, but this is correlated with the decreasing wavelength as well as narrower output cone. The narrower output cone means that marginally less of the harmonic "tail" is filtered by the Ø6 mm aperture. Various integrated in-band fluxes for the carbon resonance line [4.43 nm] are shown in figure 15. The in-band flux densities are also shown in figure 16. It is immediately and naturally apparent that with a wider bandwidth,

you have a larger angular spread in flux density as well as a larger maxima. This is because the different wavelengths in undulator radiation interfere constructively at different angles. The in-band flux density and in-band flux for other wavelengths are tabulated in Appendix A and Appendix B, respectively.

| $\lambda_\gamma$ [nm] | $\mathbf{P_{2\%BW}}$ [W] | $\mathbf{P_{4\%BW}}$ [W] | $\mathbf{P_{10\%BW}}$ [W] | $\mathbf{P_{slit}}$ [kW] |
|---|---|---|---|---|
| 7.75 | 25.6 | 50.2 | 96.7 | ~2.48 |
| 4.43 | 43.3 | 85.9 | 173.8 | ~4.13 |
| 3.1 | 51.1 | 102.6 | 222.9 | ~5.87 |
| 2.34 | 54.1 | 114.8 | 257.4 | ~6.45 |

Table 5: SPECTRA in-band power outputs and total power deposited onto a Ø6 mm aperture for $I = 500$ mA, $L = 20$ m. The power on the slit varies marginally for different bandwidth calculations.

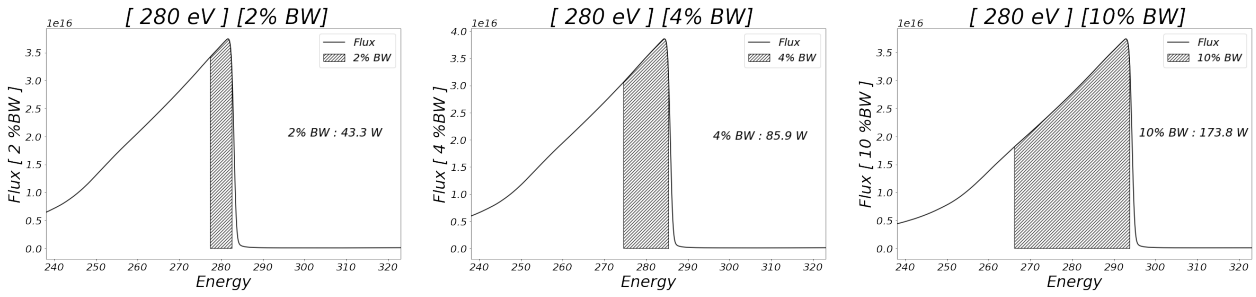


(a) (b) (c)

Figure 15: In-band flux for $\lambda = 4.43$ at (a) 2% BW, (b) 4% BW, (c) 10% BW

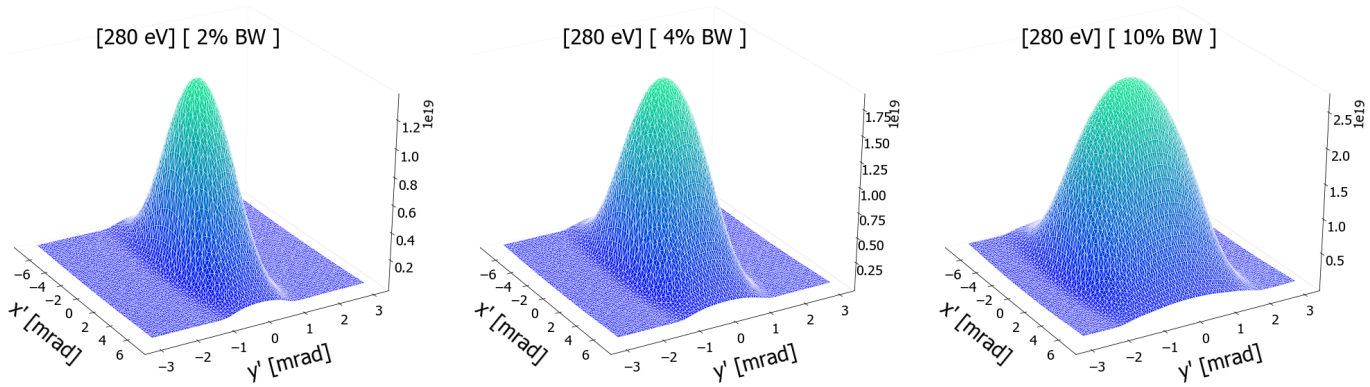


(a) (b) (c)

Figure 16: In-band flux density map for $\lambda = 4.43$ at (a) 2% BW, (b) 4% BW, (c) 10% BW

## 3.3 Conceptual footprint

Using the design lattice parameters and the beam energy it was possible to draw a scale-accurate representation of a storage ring. Also, knowing that the output flux of an undulator scales linearly with the undulator length, the representation in figure 17 includes an undulator of 40 m instead of 20 m. This is closer in length to the accelerator itself. To maximize the flux for a specific wavelength mode of interest, the length of the LINAC as well as the dipole bending radius will have to change in order to accommodate the beam energy. The dipole bending radius is determined via the magnetic rigidity equation, and the length of the linear accelerator based on the typical field gradient of ~24-25 MeV/m. This leads to a large variation in machine footprint. For example, maximizing the output flux for oxygen leads to a LINAC which is almost twice as long, and thus a bending radius which is twice as wide. A summary of machine sizes for different undulator parameters are shown in table 6.

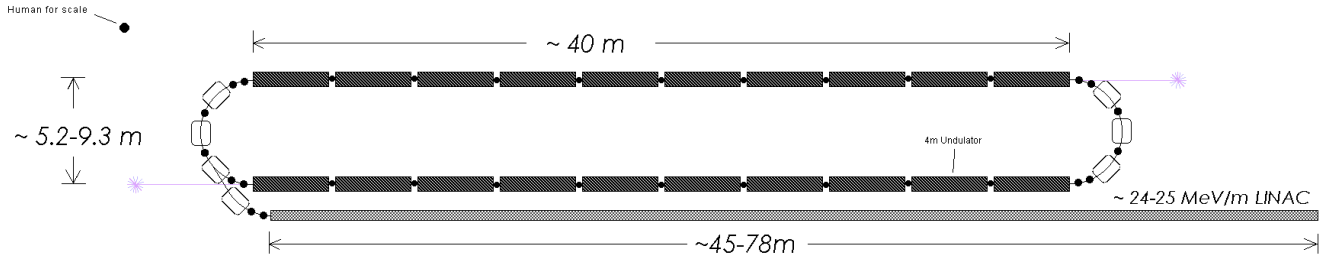


Figure 17: Conceptual footprint

| $\lambda_\gamma$ | $E_{e-}$ | $\rho$ | $L_{linac}$ | $Area$ | $\mathbf{P_{2\%BW}}$ | $\mathbf{P_{4\%BW}}$ | $\mathbf{P_{10\%BW}}$ |
|---|---|---|---|---|---|---|---|
| [nm] | [GeV] | [m] | [m] | [$m^2$] | [W] | [W] | [W] |
| 7.75 | 1.14 | 2.72 | 45.6 | 248 | 102-154 | 201-301 | 387-581 |
| 4.43 | 1.45 | 3.45 | 58.0 | 400 | 173-260 | 344-516 | 695-1042 |
| 3.1 | 1.76 | 4.19 | 70.4 | 590 | 204-307 | 412-618 | 892-1338 |
| 2.34 | 1.95 | 4.64 | 78 | 724 | 216-325 | 460-690 | 1030-1545 |

Table 6: Conceptual footprint parameters with output power at 2%, 4%, 10% BW. The lower power limit in each column is based on an aperture of Ø6 mm, with the upper power limit based on an aperture of Ø12 mm, according to figure **??**.

**Power v. cost**

Knowing that the power output is strongly dependent on the aperture size, a range is shown in figure 18 for the power v. cost curve. Using this curve one can linearly interpolate the cost for larger machines. The material cost for various power outputs at 280 eV is tabulated in table 7. Other energies are tabulated in appendix F.

| **Power** | $Cost_{2\%BW}$ | $Cost_{4\%BW}$ | $Cost_{10\%BW}$ |
|---|---|---|---|
| [kW] | [M€] | [M€] | [M€] |
| ~10 | 806 | 410 | 211 |
| ~5 | 406 | 208 | 109 |
| ~2.5 | 207 | 108 | 58 |
| ~1 | 85 | 47 | 27 |
| ~0.5 | 46 | 27 | 17 |

Table 7: Est. in-band power [280 eV] v. material cost for various bandwidths

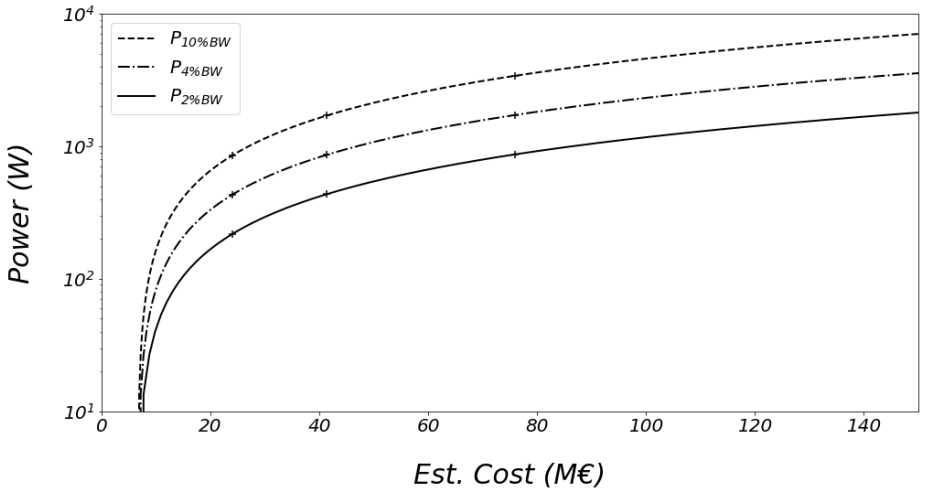


Figure 18: Est. in-band power [280 eV] v. material cost for various bandwidths

## 3.4 Discussion

It is a trend in EUVL (13.5 nm) that for every reduction in node size by 0.7x there will be a required doubling of the minimum dose due to stochastic processes (shot noise)[18]. Acceptable wafer throughput for 24 nm pitch lines is likely to require a power source of ~500W, but ideally the source should be around ~800W. The flux at this power is 5.4e+19 ph/s. The attenuation coefficient for EUVL resists is ~5 $\mu m^{-1}$[16], and correspondingly, previously studied SXL resists have shown similar values[15].

This means that in order to gain in resolution, one must match the flux for current scanners while surpassing the $\lambda/NA$ ratio defined by the Rayleigh criterion. In the case of the Carbon resonance line at 280 eV with 10% BW, this corresponds to a power of approximately 2500W. In order to have two beamlines of 2500W each, this would be a material cost of 109 M€. If we assume the optics for our system will cost ~5 M€ per beamline, the total material cost becomes ~120 M€. This would be equivalent to two conventional production line scanners (NXE:3400B), which carry a sales price of ~150 M€ each, or 300 M€ total. This seems to be attractive from a price standpoint, assuming typical sales markups. However, there remains much to be solved in terms of the optical train, including satisfaction of the Rayleigh criterion as well as optical transmission.

### Optical transmission

Given that LPP technology is the accepted standard in semiconductor manufacturing today, there must be considerable financial incentive to switch technologies, as it will take significant research and investment to deliver a production-ready machine. One of the largest takeaway from this study is that in order for conventional synchrotrons to be able to compete with FEL or LPP sources, a larger bandwidth (~10%) optical system must be utilized for the lithographic process. For example, if one can achieve 10% bandwidth instead of 2%, the machine will generate four times as much usable light.

Higher bandwidths in the soft X-Ray regime require grazing incidence mirrors. This is because the bandwidth of ML mirrors is typically in the range of 1-4%. This is in sharp contrast to a grazing incidence mirror system, which could in principle utilize the entire undulator source bandwidth. In addition, grazing incidence mirrors can achieve reflectivities of 80% or higher, whereas ML mirrors regularly see 65-70%. The differences between the two are summarized below in table 8. Naturally,

grazing incidence mirrors will require more space, and will require significant efforts in optical design in order to achieve a high NA onto the wafer stage. One possible solution is to use multiple grazing incidence axial mirrors.

| | ML Mirrors | KB Mirrors |
|---|---|---|
| Reflectivity | ~30-70% | ~50-80% |
| Bandwidth | ~1-4% | ~100% |
| NA | ~ 0.55 | ~5e-03 |

Table 8: ML v. KB Mirrors

**SXL Mirror System**

Generally speaking, in order to make gains in resolution via the Rayleigh criterion, the NA at the wafer will have to either match or be better than the current industry standard by:

$$NA_{grazing} \geq 0.55 \left( \frac{\lambda_{SXL}}{13.5nm} \right)$$

Using this relation one can determine the minimum NA required for potential SXL wavelengths as well as the corresponding half-angle. This is shown in table 9.

| $\lambda_{SXL}$ | [nm] | 7.75 | 4.43 | 3.1 | 2.34 |
|---|---|---|---|---|---|
| $NA_{min}$ | | 0.315 | 0.18 | 0.126 | 0.09 |
| $\theta_{min}$ | [°] | 18.4 | 10.4 | 7.2 | 5.2 |

Table 9: SXL wavelengths and associated minimum NA, half-angle

In order to fulfill such requirements, a special mirror system will be needed. Mirror array assemblies such as *Wolter mirrors,* which are commonly used in X-ray science, could be used to create the high-NA SXL optical systems. A proposed concept is shown below in figure 19.

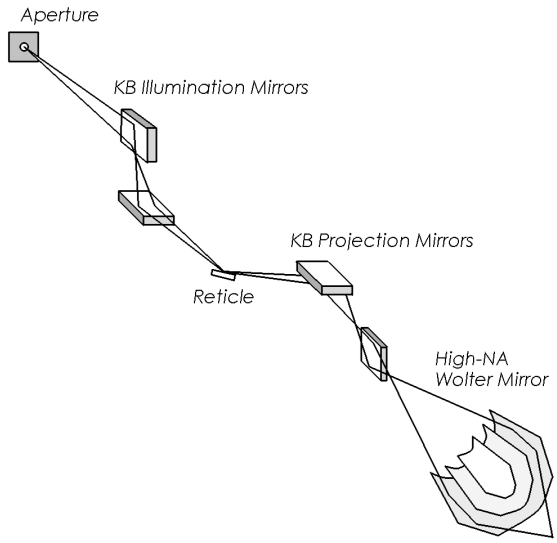


Figure 19: A conceptual optics train for high-bandwidth, high-NA SXL

# CONCLUSIONS

After an evaluation of undulator parameters and cost-per-watt study, it is clear that synchrotrons are an attractive and cost-effective source for SXL. However it is critical that a larger bandwidth is used to harvest as much useful light as possible. A larger bandwidth means that grazing incidence optics are required. This presents the additional issue of NA reduction. A larger aperture will also contribute to more power, but light contamination as well as heat problems will need to be mitigated. If a suitable optical train solution could be developed, then the next step would be the development of a test beamline to evaluate resist performance.

### Outlook

In addition to bandwidth and numerical aperture, there are other technical challenges which will remain to be solved when considering SXL wavelengths, including spatial coherence. Undulator light sources have in general a spatial coherence which is too high for lithography, and produce diffraction effects. Thus a solution will need to be found to reduce it. This can be directly mitigated with a higher power light source.

It is the author's recommendation that for the next steps for synchrotron-based lithography should focus on the optical imaging design following the undulator output. This will enable a cost evaluation of the optical components which will no doubt cost several million euros, as well as determine the feasibility of full grazing incidence based optics (including the reticle mask) for the imaging requirements of lithographic techniques. Once it is established that a high enough NA can be achieved with respect to the imaging requirements for wavelength of interest, one can begin the construction of a beamline to perform an evaluation of pitch and LER for different resist thicknesses and chemistries.

# References

[1] *EUV Lithography: State-of-the-Art Review,* N. Fu, Y. Liu, X. Ma, Z. Chenhidden, 2019

[2] *The Science and Technology of Undulators and Wigglers*, J. A. Clarke, 2004

[3] *The Physics of Particle Accelerators: An Introduction* - Klaus Wille (2000)

[4] *Power production experiments at the Test Beam Line in the CLIC Test Facility 3.* Lillestol, Reidar. (2010).

[5] *Insertion Devices: Undulators and Wigglers.* Walker, Richard. (1996)

[6] *Fundamentals of Photonics 2nd Edition*, Bahaa E. A. Saleh, (2007)

[7] *Max IV - Detailed Design Report*, 2010

[8] *Physics of laser-driven tin plasma sources of EUV radiation for nanolithography, ,* O. Versolato, *2019*

[9] *Nanofabrication for Plasmonics*, G. Lerondel, S. Kostcheev, J. Plain, 2012

[10] *Multi-patterning strategies for navigating the sub-5 nm frontier, part 1,* J. Lee, R. Kim, 2019

[11] *X-ray interactions: photoabsorption, scattering, transmission, and reflection at E=50-30000 eV, Z=1-92,* B.L. Henke, E.M. Gullikson, J.C. Davis. (1993). [https://henke.lbl.gov]

[12] *"SIMPLEX: simulator and postprocessor for free-electron laser experiments"*, T. Tanaka, (2015)

[13] *Extreme ultraviolet (EUV) sources for lithography based on synchrotron radiation,* G. Dattoli, A. Doria (2001)

[14] *https://www.imec-int.com/en/articles/imec-demonstrates-24nm-pitch-lines-with-single-exposure-euv-lithography-on-asml-s-nxe-3400b-scanner* - (retrieved 12/1/2020)

[15] *Evaluation of resist sensitivity in extreme ultraviolet/soft x-ray region for nextgeneration lithography,* T. Oyama, A. Oshima, M. Washio, (2011)

[16] *Dynamic absorption coefficients of CAR and non-CAR resists at EUV, R. Fallicaa*, J. Stowersb , A. Grenvilleb, (2019)

[17] *Enabling sub-10nm node lithography: presenting the NXE:3400B EUV scanner*, M. Kerkhof, H. Jasper, L. Levasier, (2017)

[18] *Complementary polarity exposures for cost-effective line-cutting in multiple patterning lithography,* F. T. Chen, W-S. Chen, M-J. Tsai, and T-K. Ku (2012).

[19] *BAD Basic Accelerator Design code*, D. Einfeld

# APPENDIX

## A: INTEGRATED FLUX DENSITY MAPS

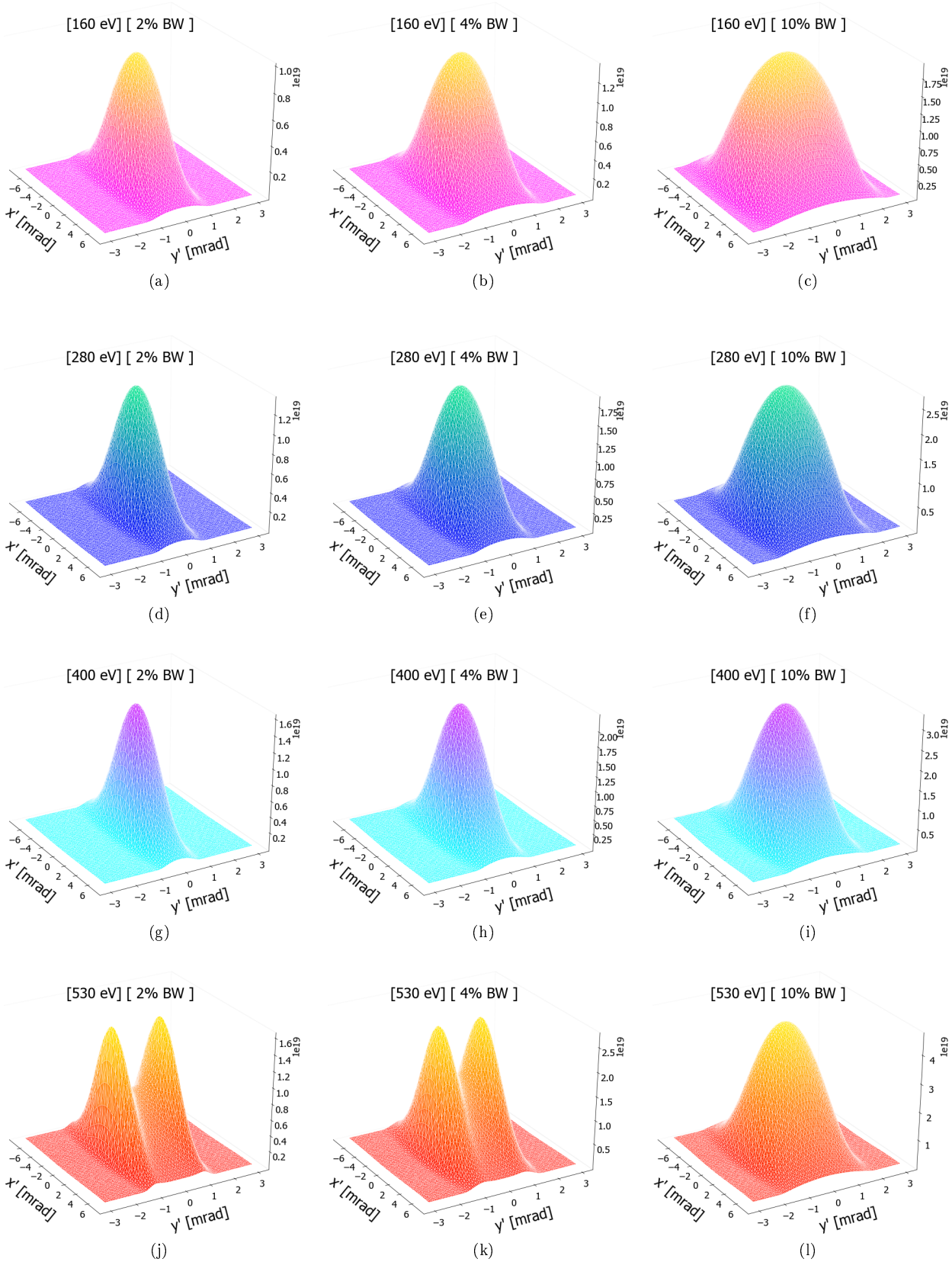


Figure 20: SPECTRA in-band flux density maps for 160 eV, 280 eV, 400 eV, 530 eV

## B: INTEGRATED FLUXES

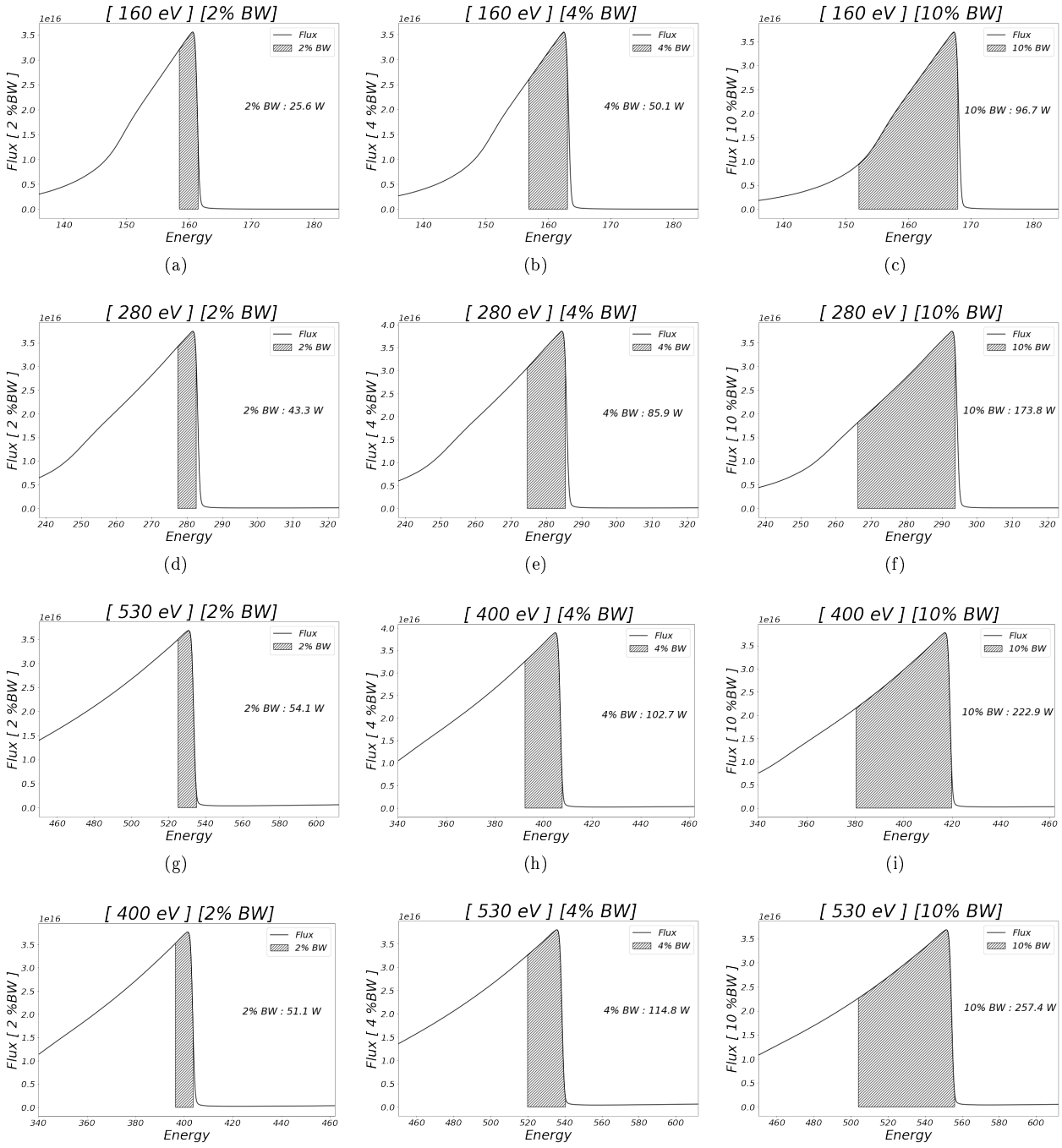


Figure 21: SPECTRA integrated in-band flux for 160 eV, 280 eV, 400 eV, 530 eV

## C: APERTURE DATA

| Ø | $\mathbf{P}_\lambda$ | $\mathbf{P_{total}}$ | $\mathbf{P_{slit}}$ | $\mathbf{P_{total} - P_{slit}}$ | $\left(\frac{\mathbf{P_{total} - P_{slit}}}{\mathbf{P_{total}}}\right)$ | $\left(\frac{\mathbf{P}_\lambda}{\mathbf{P}_{\phi=\mathbf{20mm}}}\right)$ |
|---|---|---|---|---|---|---|
| [mm] | [W] | [kW] | [kW] | [W] | [%] | [%] |
| 2 | 28.2 | 4.8 | 4.75 | 50 | 1 % | 9 % |
| 4 | 100.8 | 4.8 | 4.60 | 200 | 4 % | 32 % |
| 6 | 173.8 | 4.8 | 4.13 | 670 | 14 % | 55 % |
| 12 | 266 | 4.8 | 2.87 | 2070 | 43 % | 85 % |
| 20 | 313 | 4.8 | 0.97 | 3830 | 80 % | 100 % |
| *none* | 354 | 4.8 | 0 | 4800 | 100 % | 113 % |

Table 10: SPECTRA in-band power (10% BW), total power, power on the slit for various aperture sizes for 280 eV

## D: MIRROR BANDWIDTHS

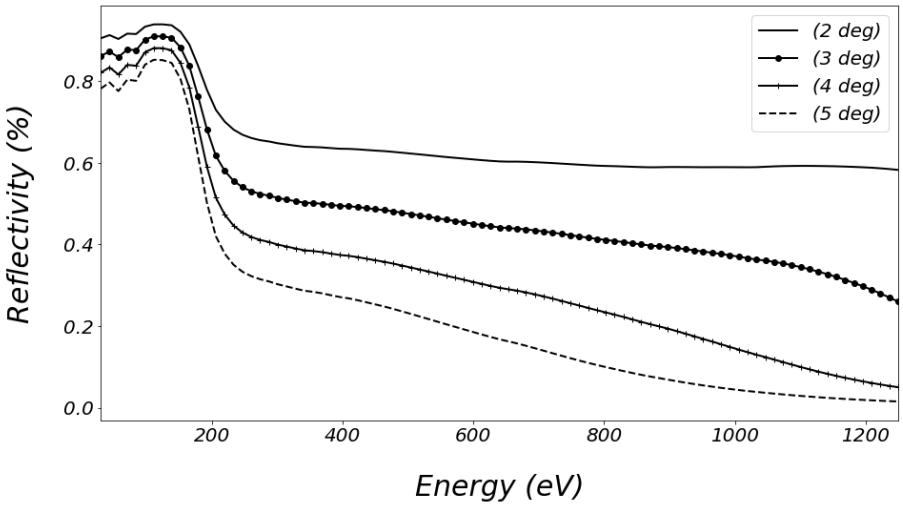


(a)

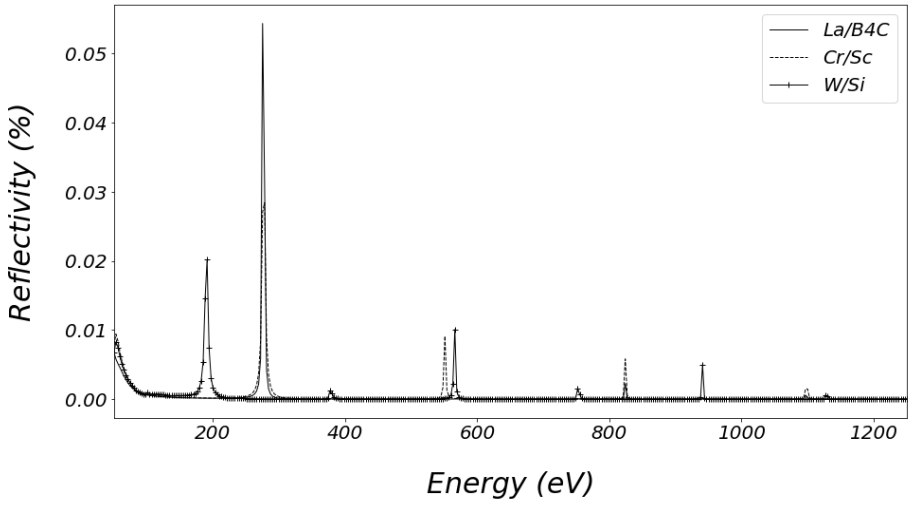


(b)

Figure 22: Typical reflectivity v. energy curves for (a) Au coated grazing incidence mirror and (b) ML mirrors at normal incidence [11]

## E: UNDULATOR PARAMETERS SETS

| $E_{e-}$ | $\lambda_\gamma$ | $K$ | $B$ | $\lambda_u$ | $\Phi_{1st}$ | $\mathbf{P_{1st}}$ | $\mathbf{P_{total}}$ |
|---|---|---|---|---|---|---|---|
| [GeV] | [nm] | | [T] | [cm] | [ph/s @ 0.1%BW] | [W @ 0.1%BW] | [kW] |
| 1.14 | 7.75 | 1.183 | 0.4 | 3.17 | 2.89e+16 | 0.75 | 2.62 |
| 1.45 | 4.43 | 1.163 | 0.415 | 3.0 | 3.01e+16 | 1.37 | 4.58 |
| 1.76 | 3.1 | 1.182 | 0.415 | 3.05 | 3.01e+16 | 1.94 | 6.77 |
| 1.95 | 2.34 | 1.121 | 0.4 | 3.0 | 2.92e+16 | 2.50 | 7.70 |

Table 11: Resolved circular undulator parameters used for 2% BW simulations in SPECTRA ($I = 500$ mA, $L = 20$ m, gap = 12 mm)

| $E_{e-}$ | $\lambda_\gamma$ | $K$ | $B$ | $\lambda_u$ | $\Phi_{1st}$ | $\mathbf{P_{1st}}$ | $\mathbf{P_{total}}$ |
|---|---|---|---|---|---|---|---|
| [GeV] | [nm] | | [T] | [cm] | [ph/s @ 0.1%BW] | [W @ 0.1%BW] | [kW] |
| 1.16 | 7.6 | 1.2 | 0.4 | 3.22 | 2.89e+16 | 0.76 | 2.74 |
| 1.49 | 4.34 | 1.2 | 0.43 | 3.0 | 3.10e+16 | 1.42 | 5.18 |
| 1.78 | 3.05 | 1.2 | 0.43 | 3.0 | 3.10e+16 | 2.02 | 7.37 |
| 2.0 | 2.3 | 1.16 | 0.42 | 3.0 | 3.01e+16 | 2.59 | 8.72 |

Table 12: Resolved circular undulator parameters used for 4% BW simulations in SPECTRA ($I = 500$ mA, $L = 20$ m, gap = 12 mm)

| $E_{e-}$ | $\lambda_\gamma$ | $K$ | $B$ | $\lambda_u$ | $\Phi_{1st}$ | $\mathbf{P_{1st}}$ | $\mathbf{P_{total}}$ |
|---|---|---|---|---|---|---|---|
| [GeV] | [nm] | | [T] | [cm] | [ph/s @ 0.1%BW] | [W @ 0.1%BW] | [kW] |
| 1.14 | 7.38 | 1.18 | 0.42 | 3.05 | 3.00e+16 | 0.81 | 2.82 |
| 1.49 | 4.21 | 1.17 | 0.42 | 3.02 | 3.01e+16 | 1.42 | 4.82 |
| 1.78 | 2.96 | 1.17 | 0.42 | 3.02 | 3.01e+16 | 2.02 | 6.87 |
| 1.99 | 2.24 | 1.12 | 0.4 | 3.0 | 2.91e+16 | 2.59 | 8.00 |

Table 13: Resolved circular undulator parameters used for 10% BW simulations in SPECTRA ($I = 500$ mA, $L = 20$ m, gap = 12 mm)

## F: POWER V. COST EVALUATIONS

| **Power** [kW] | $Cost_{2\%BW}$ [M€] | $Cost_{4\%BW}$ [M€] | $Cost_{10\%BW}$ [M€] |
|---|---|---|---|
| ~10 | 1372 | 697 | 391 |
| ~5 | 688 | 352 | 198 |
| ~2.5 | 348 | 179 | 101 |
| ~1 | 143 | 76 | 43 |
| ~0.5 | 75 | 41 | 24 |

Table 14: Est. in-band power [160 eV] v. material cost for various bandwidths

| **Power** [kW] | $Cost_{2\%BW}$ [M€] | $Cost_{4\%BW}$ [M€] | $Cost_{10\%BW}$ [M€] |
|---|---|---|---|
| ~10 | 806 | 410 | 211 |
| ~5 | 406 | 208 | 109 |
| ~2.5 | 207 | 108 | 58 |
| ~1 | 85 | 47 | 27 |
| ~0.5 | 46 | 27 | 17 |

Table 15: Est. in-band power [280 eV] v. material cost for various bandwidths

| **Power** [kW] | $Cost_{2\%BW}$ [M€] | $Cost_{4\%BW}$ [M€] | $Cost_{10\%BW}$ [M€] |
|---|---|---|---|
| ~10 | 683 | 343 | 162 |
| ~5 | 344 | 174 | 84 |
| ~2.5 | 176 | 90 | 45 |
| ~1 | 74 | 40 | 22 |
| ~0.5 | 40 | 23 | 14 |

Table 16: Est. in-band power [400 eV] v. material cost for various bandwidths

| **Power** [kW] | $Cost_{2\%BW}$ [M€] | $Cost_{4\%BW}$ [M€] | $Cost_{10\%BW}$ [M€] |
|---|---|---|---|
| ~10 | 648 | 308 | 141 |
| ~5 | 327 | 157 | 74 |
| ~2.5 | 167 | 82 | 40 |
| ~1 | 70 | 37 | 20 |
| ~0.5 | 38 | 21 | 13 |

Table 17: Est. in-band power [530 eV] v. material cost for various bandwidths